Attenuation length in ion-induced kinetic electron emission: A key to an understanding of angular-dependent yields

Klaus Wittmaack

Helmholtz Zentrum München, Institute of Radiation Protection, 85758 Neuherberg, Germany

(Received 18 September 2014; revised manuscript received 22 January 2015; published 26 March 2015)

The mean attenuation length, $\langle L\rangle$, of electrons emitted from ion bombarded solids was derived from measured angular-dependent electron yields $\gamma(\theta)$ in combination with Monte Carlo simulations of inelastic (electronic) energy deposition. The transport controlled contributions of excited electrons to the measured electron yields were derived as the integral g_L over $S_e\exp(-z/L)$, where $S_e(\theta,z)$ is the electronic energy deposition and z the depth from the surface. The unknown attenuation length $L \equiv \langle L\rangle$ reflects the average over the energy spectrum and the angular distribution of those internally excited electrons that can reach the solid-vacuum interface and overcome the surface barrier. To determine L, the ratios $g_L(\theta)/g_L(0)$, calculated for $0 \leqslant L \leqslant 10$ nm, were compared with measured yield ratios $\gamma(\theta)/\gamma(0)$ for a wide variety of projectile-target combinations and impact energies between 1 and 50 keV (velocity-proportional electronic stopping). The procedure works well at angles at which $S_e(\theta,z)$ decreases smoothly in the depth region between 1 and 3 nm. The result is $\langle L\rangle = 1.5 \pm 0.3$ nm, a number basically in accordance with expectation based on estimated data for the inelastic mean free path of low-energy electrons (<25 eV) but a factor of 10 lower than the numbers recently advocated (10–15 nm) to rationalize "internal" electron yields observed with metal-insulator-metal sandwich structures.

DOI: 10.1103/PhysRevB.91.115434 PACS number(s): 79.20.Rf, 34.35.+a, 34.50.Bw

I. INTRODUCTION

Ions or neutrals injected into solid samples lose their energy in a series of elastic ("nuclear") and inelastic ("electronic") collisions with target atoms and electrons. A very valuable method of studying the various processes associated with electronic excitation is to measure yields and energy spectra of emitted electrons. The main principles and mechanisms of kinetic electron emission (KEE) have been reviewed from different perspectives [1–3]. More recently researchers explored finer details, such as the mechanism of plasmon assisted electron emission [4] and the importance of electron promotion [5]. Several problems, however, remained unsolved, one being the poorly known transport of excited electrons to the bombarded surface.

The electrons contributing most to KEE yields have (external) energies $E_{ex} < 10$ eV, equivalent to internal energies $E = E_{ex} + E_F + \Phi < 20$ to 25 eV [2], where E_F denotes the Fermi energy and Φ the work function of the sample. Studies on electron transport phenomena at higher energies, $50 < E < 2000$ eV, were stimulated by the widespread interest in the use of x-ray photoelectron and Auger electron spectroscopy for surface analytical applications. One needs to distinguish between (i) the inelastic mean free path (IMFP), λ_{in}, determined theoretically from a combination of optical data and scattering probabilities [6], and (ii) the mean free path for elastic electron scattering, λ_{el} [7]. The parameter of concern in experimental work is the attenuation length (AL), L [8,9], which involves the assumption that, in response to the joint action of elastic and inelastic scattering, the number of electrons, excited to energy E at depth z, will be reduced by a factor $\exp(-z/L)$ after transport to the surface at $z = 0$. The AL is generally different from the IMFP [9]; in cases of common interest L is typically 20%–30% lower than λ_{in} [10]. Depending on the element, the IMFP exhibits a minimum between 0.4 and 0.6 nm in the range $50 < E < 100$ eV [6,10]. Below 50 eV the IMFPs are predicted to increase, to between 1 and 2 nm at 10 eV [6,10]. Interest in the low-energy region is due to the recent finding that the IMFP may be determined from x-ray absorption fine structures [11] and the low-energy electron reflectivity of ultrathin films [12].

The present work was originally motivated by another open question in KEE: What is the origin of the long-known experimental finding [13–16] that the response of electron yields, γ, to variations of the impact angle θ can vary drastically, depending on the projectile energy E_0 and the projectile-target combination? Not knowing the AL in any detail, experimental data for polycrystalline metals were previously evaluated by either setting $L \equiv \langle L\rangle = 2$ nm [13] or $\langle L\rangle = 0$ [14,15], the notation $\langle L\rangle$ being meant to indicate that the AL in KEE reflects averaging over internal energies and angles. Detailed $\gamma(\theta)$ data for single-crystal Cu bombarded with 5–10-keV Ar^+ could be reproduced using a semiempirical molecular dynamics model, to arrive at a best fit with $\langle L\rangle = 1.8\pm0.2$ nm [17]. Other recent studies, however, on the novel issue of "internal" electron emission in metal-insulator-metal sandwich layers [18–20], showed unexpectedly high yields which could only be explained assuming that the AL was as large as 10–15 nm. The huge discrepancy between the results of different types of KEE studies calls for a clarification.

II. DATA BASIS AND CONCEPT OF EVALUATION

This study examined angular-dependent ion-induced electron yields, $\gamma(\theta)$, reported by three different groups as well as results obtained in course of the present work. The impact angle θ is measured with respect to the surface normal of the bombarded sample. Examples of normalized yields $\gamma(\theta)/\gamma(0°)$, are compiled in Fig. 1 for Xe^+ on Au [13], Xe^+ on Al [14], Xe^+ on Cu [15], O^+ on Al [16], O^+ on Au, and Ne^+ on Au (this work; measurements performed with the same setup as in Ref. [16]). The data in the region $0° \leqslant \theta < 60°$ can often be approximated by $\gamma(\theta)/\gamma(0°) = \cos^{-p}\theta$ [13–16], with

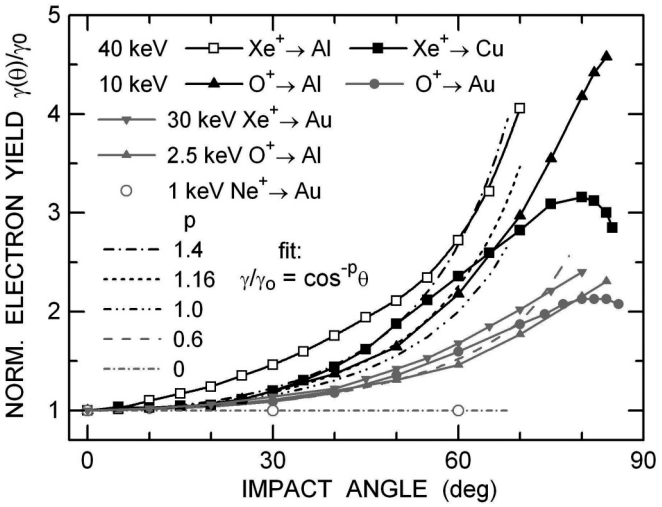

FIG. 1. Normalized electron yields versus the primary-ion impact angle. From Refs. [13–16] and this work. The gray data highlight "subcosine" cases for which $p < 1$. Yields due to potential electron emission were not subtracted from the raw data.

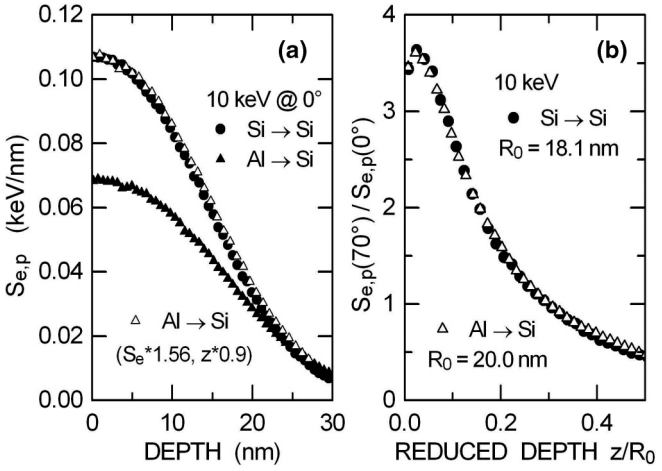

FIG. 2. (a) Depth dependence of the electronic energy deposition by 10-keV Si and Al normally incident on Si, as calculated with SRIM-2006 (solid symbols). The open triangles were derived by applying the specified scaling factors to the raw Al data. (b) Ratios of the energy deposition of Si and Al in Si at 70° and 0° versus the reduced depth z/R_0, with R_0 denoting the mean projectile range at normal incidence.

exponents p varying from 0 (1-keV Ne^+ on Au) to 1.4 (40-keV Xe^+ on Cu). Sometimes an even more pronounced, non–cosine θ dependence was observed, as for 40-keV Xe^+ on Al in Fig. 1. The differences in θ dependence were discussed along various lines [1–3,13–15], but a generally accepted model could not yet be established.

Here, the starting point of the data evaluation was the hypothesis that the observed θ dependence of electron yields is solely determined by the depth distribution of electronic excitation and the AL of the excited electrons. To calculate the energy deposition, use was made of the Monte Carlo code SRIM-2006.02 [21]. The code has been employed before in models of internal electron emission [18–20] without questioning the reliability of the code. Prior work showed that the employed electronic stopping cross sections were often significantly or even strongly at variance with experimental data [22–24]. Fortunately, however, the simulated data discussed below involve only *ratios* of differential electronic energy losses at different angles θ so that systematic errors might be expected to be distinctly less pronounced than in the range calculations.

Inspection of the impact-energy dependence of energy losses, $S = -dE/dz$ at the surface ($z = 0$) showed that SRIM-2006 assumes velocity-dependent electronic stopping in accordance with established concepts due to Lindhard *et al.* (LSS) [25]. Two examples of depth differential electronic energy losses by projectiles, $S_{e,p}(z)$, are shown in Fig. 2(a) as solid symbols. At 10 keV, $S_{e,p}(z = 0)$ according to LSS should be only about 3% higher for Si-Si than for Al-Si. By contrast, the difference amounts to as much as 56% according to SRIM-2006, for unknown reasons. On the other hand, the difference in the most probable projected range, $R_0 \equiv R(\theta = 0)$, is only 10%; R_0(Si-Si)= 18.1 nm versus R_0(Al-Si)= 20.0 nm. The much smaller effect on the range is due to the fact that, in the case considered, nuclear stopping is the dominant source of energy loss, a factor of ∼4.5 stronger than electronic stopping.

Depth-dependent ratios of electronic stopping, $S_e(\theta)/S_e(0°)$ are shown in Fig. 2(b) for $\theta = 70°$. In the evaluations presented below, such ratios will serve as the key to determining the attenuation length. If the 10% difference in range is removed by way of presenting the ratios as a function of the reduced depth z/R_0, the uncorrected (!) ratios $S_e(70°)/S_e(0°)$ for Si-Si and Al-Si are seen to be essentially indistinguishable. The same kind of result was obtained at other angles and for 10- and 20-keV Al-Al and Si-Al. These findings imply that the relative contribution of a possible error in electronic stopping to the total energy loss is the same at different impact angles. Therefore, the error disappears if S_e ratios are considered.

III. RESULTS AND DISCUSSION

A. Basic features of energy deposition, backscattering, and projectile ranges

To appreciate similarities and differences in electronic energy deposition for different projectile-target combinations and different impact energies, a brief summary of results obtained with SRIM should be helpful. The total inelastic loss, $S_{e,\Sigma}$, is the sum of the contributions $S_{e,p}$ and $S_{e,r}$ due to direct excitation by projectiles (subscript p) as well as by target-atom recoils (r). Two characteristic examples of depth and impact-angle-dependent energy losses, $S_e(z,\theta)$, are presented in Fig. 3 for $\theta = 0°$ and 70°. The relative contributions of $S_{e,p}$ and $S_{e,r}$ to $S_{e,\Sigma}$ are seen to depend strongly on the projectile-target combination. Whereas the recoil contributions to electronic stopping are small for light elements, Fig. 3(a), they become dominant for heavy elements, Fig. 3(b). Another important difference is that, at $\theta = 0°$ and angles not too far off normal, the maxima of $S_{e,p}$ and $S_{e,r}$ are observed at distinctly different depths, either right at the surface ($S_{e,p}$) or well away from the surface ($S_{e,r}$). The "delayed" contribution of recoils is due

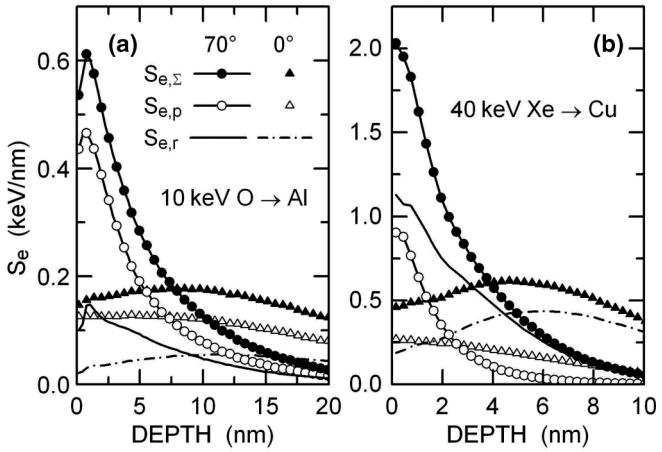

FIG. 3. Depth distribution of inelastic electronic energy losses of (a) 10-keV O on Al and (b) 40-keV Xe on Cu, for different impact angles, as calculated with SRIM-2006 [number of projectiles $N = 30\,000$; step width $\Delta z = 0.3$ nm; every second data point skipped in (a) for clarity]. The total losses and the distinctly different contributions due to projectiles and recoils are shown separately (subscripts Σ, p, and r, respectively).

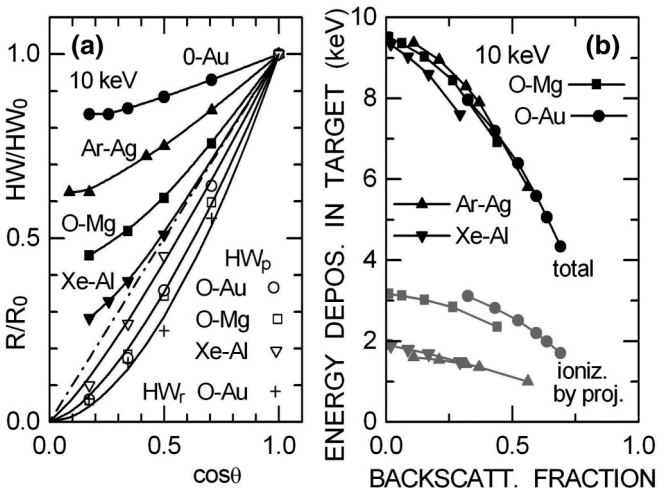

FIG. 5. (a) Normalized ranges (solid symbols) and half width of the distributions of electronic energy deposition (open symbols and crosses) for different projectile-target combinations versus the cosine of the impact angle. The dash-dotted line denotes direct proportionality. (b) Integral electronic and total energy deposition versus backscattering coefficient, for four different projectile-target combinations. The impact angles in (b) are the same as in (a).

to the fact that they first need to be generated by projectile impact before they become effective in producing electronic excitation.

Previous attempts to rationalize the angular dependence of ion-induced electron yields involved the idea that the path length of the projectile in the sample is an important parameter [1,2,20]. The results of the SRIM calculations, however, provided evidence that the depth-dependent distributions $S_{e,p}$ and $S_{e,r}$ are poorly correlated with the changes of the projectile range distributions. The data of Fig. 4(a) show how close to the surface electronic energy deposition may take place if 10-keV O projectiles are incident on Au at an impact angle of 80°. The corresponding range distributions, on the other hand, exhibit only a very small shift towards the surface as the impact angle is changed from 0° to 80°; see Fig. 4(b). This rather extreme insensitivity to changes of the impact angle is due to the fact that, in response to the large mass ratio M_2/M_1 of target (M_2) and projectile atoms (M_1), O projectiles hitting Au atoms frequently experience pronounced angular scattering, as soon as they have entered the target, irrespective of the initial angle θ. This has the consequence that the backscattering coefficient β is already as large as 0.33 at $\theta = 0°$, to increase to 0.69 at 80° [the integrals over the range distributions in Fig. 4(b) equal the retention coefficient $1–\beta$].

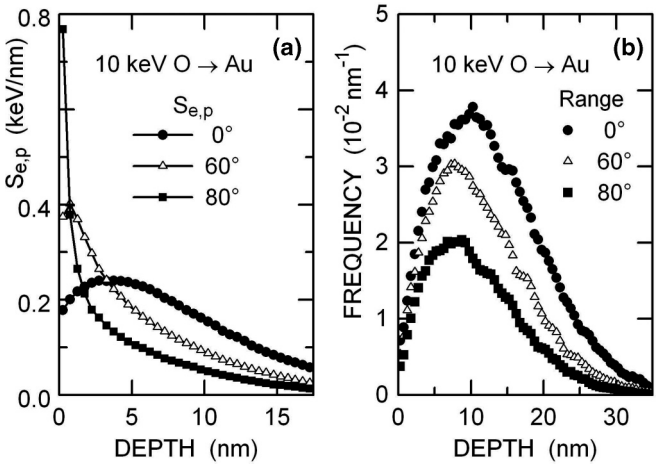

FIG. 4. Distributions of (a) electronic energy deposition due to projectiles and (b) projectile ranges of 10-keV O in Au at different impact angles, as calculated with SRIM-2006 ($N = 50\,000$; step width $\Delta z = 0.5$ nm). Three-point smoothing of the raw data applied in (b).

With decreasing mass ratio M_2/M_1 the normalized ranges R/R_0 decrease more strongly with increasing θ (decreasing $\cos\theta$) than for O-Au, but a relation of the form $R/R_0 = \cos\theta$ is only observed for heavy projectile impact on light-atom targets, like Xe on Al, and even then limited to $\theta < 60°$; see Fig. 5(a). Also shown are examples of the angular-dependent changes in half width (HW) of the distributions of electronic energy deposition (projectiles: open symbols; recoils: crosses). The lines through the open symbols and crosses represent fit functions of the form $\cos^p\theta$, with $p = 1.2$, 1.5, and 1.8. The pronounced difference compared to the angular dependence of ranges is evident again.

Owing (mostly) to the fact that backscattered projectiles carry a sizable fraction of their initial energy as they leave the target [26], the total (integral) amount of energy deposited in the sample decreases with increasing backscattering coefficient; see Fig. 5(b). The "reflected energy" is not available for exciting electrons in the target. Hence angular-dependent changes in KEE yields will be distinctly smaller than they could be in the absence of backscattering. The data in Fig. 5(b) also show that the contribution of electronic energy deposition by projectiles to the total loss is moderate or even small, but depends significantly on the mass ratio M_2/M_1.

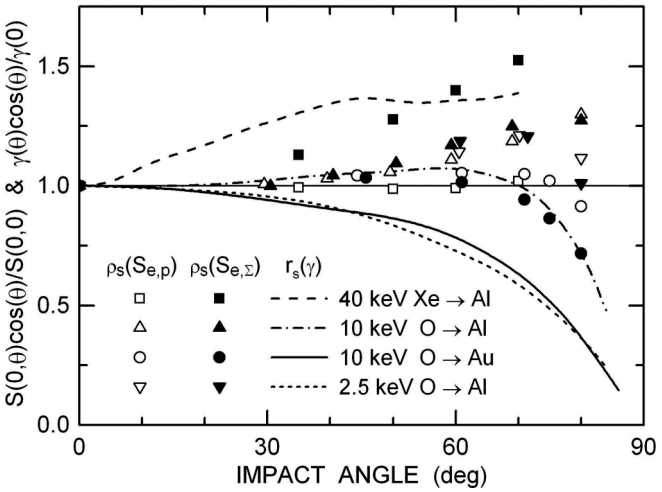

FIG. 6. Scaled ratios of the calculated electronic energy losses at the bombarded surface (projectiles: open symbols; total losses: solid symbols) versus the impact angle. Scaled ratios of KEE yields are shown for comparison (lines).

B. Electron-yield ratios for emission from the top surface layer

The most straightforward approach to comparing calculated electronic energy losses with measured KEE yields is to assume that emitted electrons originate only from the outermost layer of the bombarded sample, set equal to the first depth interval in the calculations, $0 \leqslant z \leqslant 0.12-0.3$ nm, depending on the depth of excitation. The respective energy loss is denoted $S_e(0,\theta)$. This ansatz is analogous to an approach used before [14,15]. To ease discussion we consider scaled ratios $\rho_s(Se) = S_e(0,\theta)\cos\theta/S_e(0,0)$, shown in Fig. 6 as open and solid symbols (projectile and total losses, respectively). The corresponding electron yields, taken from Fig. 1, were also converted to scaled ratios, $r_s(\gamma) = \gamma(\theta)\cos\theta/\gamma(0)$, represented by different lines. In terms of the angular dependence, the calculated loss ratios exhibit a familiar variability, from mostly "over cosine" ($p > 1$) to "under cosine" ($p < 1$). With the exception of 40-keV Xe-Al at θ<55°, $\rho_s(S_e)$ is seen to be larger than $r_s(\gamma)$, often much larger. Depending on the projectile-target combination, the difference between the two ratios increases with increasing impact angle. The conclusion to be drawn from (most of) the data in Fig. 6 is clear: Taking into account only the outermost layer, one (strongly) overestimates the angular dependence of electron yields on electronic energy deposition.

C. Electron-yield ratios controlled by attenuation

According to the results of Fig. 3, $S_{e,p}(70°)$ and $S_{e,r}(70°)$ start to decrease at depths between 0.3 and 1 nm, but $S_{e,p}(0°)$ and $S_{e,r}(0°)$ stay roughly constant or even increase for z up to about 6 nm. Hence, at shallow depths, the ratios $\rho(S_e) = S_e(z,\theta)/S_e(z,0)$ decrease rapidly with increasing z. In order to achieve agreement between calculated ratios and $r(\gamma) = \gamma(\theta)/\gamma(0°)$ one must take an appropriate average over the energy deposition within a suitable depth interval below the surface. This kind of averaging can be achieved by applying the standard approach to electron transport in KEE [1–3,7,13–15]: Assuming the measured yield to be

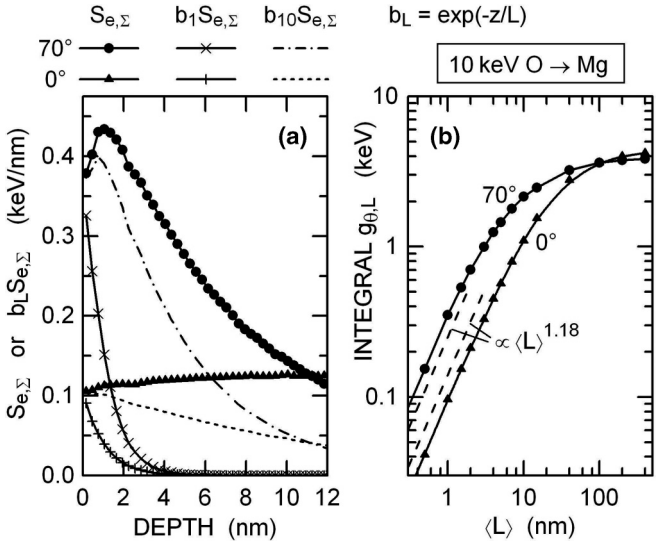

FIG. 7. (a) Depth dependence of the total electronic energy deposition for impact of 10-keV O on Mg at normal and oblique incidence (solid symbols). The same data are also shown after application of an exponential attenuation factor, with $L = 1$ and 10 nm. (b) Integral electron-yield parameter $g(\theta,L)$ versus L, for two different impact angles.

proportional to an integral $g_{L,\theta}$ in the form

$$g_{\theta,L} = g(\theta,L) = \int dz S_e(z,\theta)\exp(-z/L), \qquad (1)$$

the electron-yield ratio $r(g_L)$, predicted with L as an input parameter, reads

$$r(g_{\theta,L}) = g_{\theta,L}/g_{0,L}. \qquad (2)$$

Integration in Eq. (1) should cover the depth interval $0 \leqslant z \leqslant z_m$, where z_m is an appropriate upper limit in depth at which electronic excitation has fallen to a negligible level. Note that here and in previous approaches the probability for an excited electron to overcome the surface barrier is (was) assumed to be independent of the impact angle.

To illustrate the very pronounced effect of the exponential attenuation term on the availability of electrons at the surface, Fig. 7(a) shows a comparison of $S_{e,\Sigma}(z,\theta)$ and $S_{e,\Sigma}(z,\theta)b_L(z) = S_\Sigma(z,\theta)\exp(-z/L)$ for $\theta = 0°$ and 70°, assuming two extreme cases of the mean attenuation length, $L = 1$ and 10 nm. The data were calculated for 10-keV O incident on Mg. In the case $L = 1$ nm, only a very small fraction of all generated electrons will contribute to the externally measured yield and of those detected, between 87% (0°) and 89% (70°) originate from depths less than 2 nm. This has the consequence that the efficiency of ion impact in ejecting electrons from the sample will be rather poor. Integral yields $g_{\theta,L}$ derived according to Eq. (1) are compiled in Fig. 7(b). Compared to the total energy deposited on average into electronic excitation at 0° (4.42 keV) only 96 eV (2.2%) would be utilized for KEE (ignoring the escape probability). If, on the other hand, L were as large as 10 nm, the efficiency would increase by more than an order of magnitude because in that case 1.1 keV of electronic excitation were available for KEE. Note that the calculated electron yield is not directly

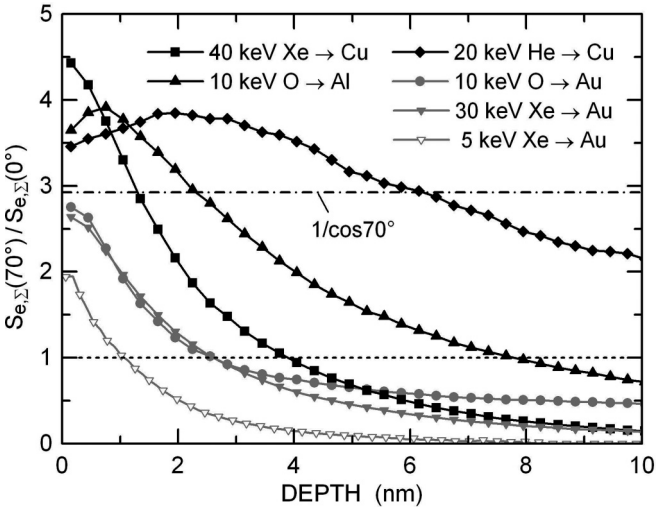

FIG. 8. Depth dependence of calculated ratios of total electronic energy deposition at 70° and 0°, for a variety of projectile-target combinations and impact energies. The black and gray data represent cases in which the angular dependence of electron yields was found to be (inversely) over cosine and under cosine, respectively, see Fig. 1.

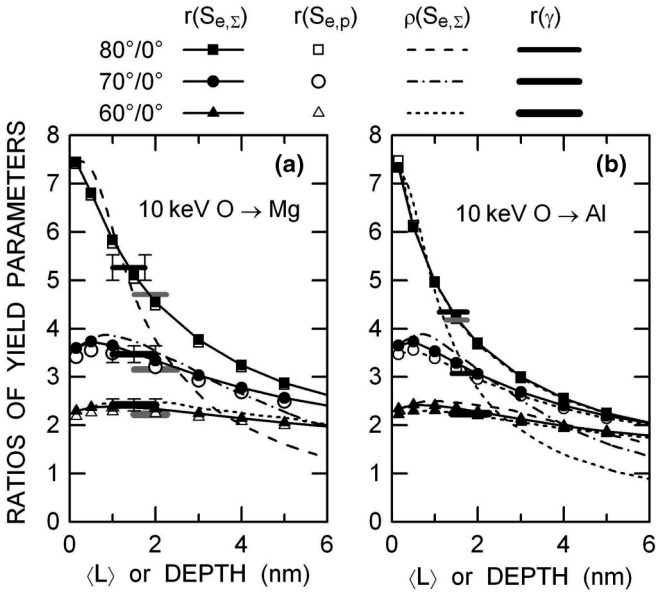

FIG. 9. Calculated electron-yield ratios r versus the assumed attenuation length $\langle L\rangle$, for different angles of projectile impact; 10-keV O on (a) Mg and (b) Al (Ref. [16]). Solid symbols: total energy deposition, open symbols: projectile contribution. The lines without symbols represent depth-dependent ratios in total energy deposition, ρ, not including attenuation. Horizontal bars: electron-yield ratios derived from experimental data, corrected for potential emission, $\gamma_{\mathrm{PEE}}(\mathrm{Mg}) = 0.12$, $\gamma_{\mathrm{PEE}}(\mathrm{Al}) = 0.04$; the gray bars show ratios of raw (uncorrected) data.

proportional to L, as assumed previously [2], but may be approximated, in limited regions of L, by $g_{\theta,L} \propto L^q$. For $L < 1.5$ nm, $q \cong 1.18$; see Fig. 7(b). The deviation from $q = 1$ reflects the fact that $S_{e,\Sigma}(z)$ is not constant but changes with depth, increasing initially; see Fig. 7(a).

Prior to examining angular-dependent ratios $r(g_{\theta,L})$ in detail, it is worth noting that the electron-yield data under study cover a variety of bombardment parameters and target materials. The expected differences in the depth distributions of electronic energy deposition are depicted in Fig. 8 in the form of ratios $S_{e,\Sigma}(z,70°)/S_{e,\Sigma}(z,0°)$. The half widths of these distributions range from 1 to about 10 nm. The differences in width can be expected to be carried over, directly or in modified form, if ratios including attenuation are considered (see below). The other important result is the correlation with the electron-yield ratios in Fig. 1. The over-cosine angular dependence $\gamma(\theta)/\gamma(0°)$ for 40-keV Xe-Cu and 10-keV O-Al, for example, is mirrored in Fig. 8 in that $S_{e,\Sigma}(z,70°)/S_{e,\Sigma}(z,0°)$ significantly exceeds the cosine limit $1/\cos 70°$ (dash-dotted line), from the surface to a depth between 1.5 and 2 nm. Likewise, there is an analogy in the under-cosine dependence for 10-keV O-Au and 30-keV Xe-Au (gray symbols).

The ratio $g_{70,L}/g_{0,L}$ changes with increasing L. This effect, not immediately evident on the logarithmic scale in Fig. 7(b), is the clue to determining L, as illustrated in Figs. 9–12 for a variety of projectile-target combinations and oblique impact angles between 60° and 80°. The calculated integral yield ratios $r(S_{e,L})$ are shown as solid and open symbols, representing total and partial (projectile) energy deposition, respectively. To illustrate the effect of attenuation, the raw ratios $\rho(S_{e,z})$ are included (dashed or dash-dotted lines). The thick horizontal bars denote measured KEE yield ratios $r(\gamma)$, corrected for potential electron emission where necessary (black: with correction; gray: without correction).

As to the results of Fig. 9, we first note the similarity of the data for 10-keV O incident on either Mg or Al, panels (a) and (b), respectively. The main difference is that, due to the lower nuclear and electronic stopping power, the yield ratios $r(S_{e,L})$ at equivalent height are located at larger depth in Mg than in Al. For impact angles $\theta \leqslant 70°$, the ratios $r(S_{e,L})$ initially increase slightly with increasing L, pass through a maximum, and then decrease. At 80° a maximum is no longer detectable and the falloff with increasing L is very pronounced. This rapid falloff has the advantage that the L value producing best agreement between $r(S_{e,\Sigma,L})$ and $r(\gamma)$ is very well defined, except for the uncertainty associated with the potential electron yield γ_{PEE} [27]. Following common practice, this yield was subtracted from the total measured yields so as to derive, as accurately as possible, the "'true" KEE yields and yield ratios for impact of neutral projectiles. In the case of Mg the correction is significant ($\gamma_{\mathrm{PEE}} = 0.12$). Without correction, $L(80°) =$ 1.9 nm, with correction, 1.4 nm. Similar results were obtained at 70° and 60°. For Al the derived L values range between 1.4 and 1.9 nm. The remarkable conclusion is that, within experimental accuracy, the attenuation lengths producing best agreement between calculated and experimental yields are the same for impact angles between 60° and 80°.

Several additional comments on the data in Fig. 9 are in place. (i) The differences between $r(S_{e,\Sigma,L})$ and $r(S_{e,p,L})$ are very small. This is due to the fact that the contribution of recoils to the total ionization is relatively small; see Fig. 3(a). Such cases are not suited to deciding whether or not the recoil contribution should be included in the calculation. (ii) At moderately oblique impact angles, like 60° or 70°, both the experimental and the calculated yield ratios need

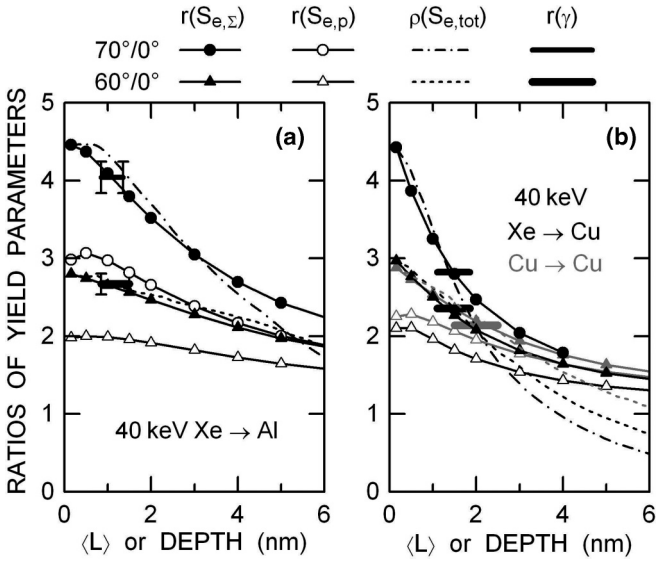

FIG. 10. The same as Fig. 9, but for (a) 40-keV Xe on Al (Ref. [14]) and (b) 40-keV Xe or Cu on Cu (Ref. [15]). Note the pronounced difference in the calculated yield ratios for total and projectile-only ionization. Corrections were assumed to be negligible in (a), $\gamma_{\mathrm{PEE}} \leqslant 0.03$, or not required in (b). To avoid too much overlap of data, $r(S_{e,p,70^\circ})$ is not shown in (b).

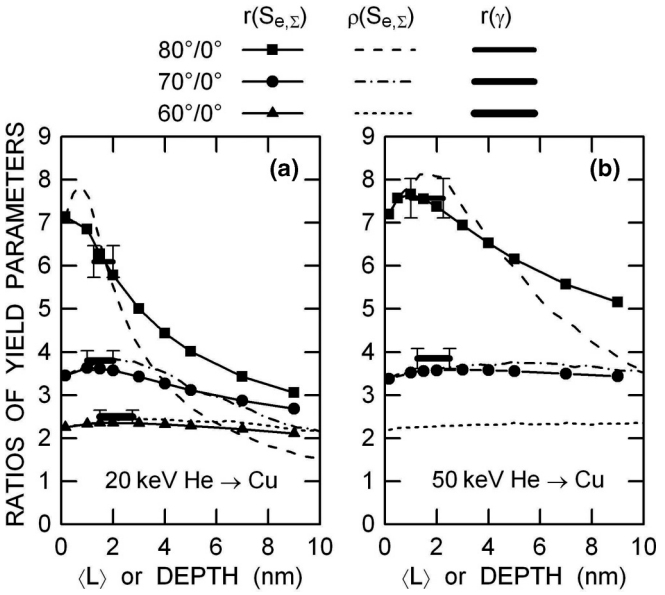

FIG. 11. The same as Fig. 9, but for He on Cu, (a) 20 keV and (b) 50 keV. Experimental data corrected for potential emission, $\gamma_{\mathrm{PEE}} = 0.24$ (Ref. [13]).

to be highly accurate for a safe evaluation of L. The error bars added to the experimental data in Fig. 9(a) represent an estimated uncertainty of ±5%. This must be considered an upper tolerable limit for the kind of evaluation of interest here. (iii) In the depth range and L range covered by the data in Fig. 9 the difference between the "attenuated" integral yield ratios $r(S_{e,\Sigma,L})$ and the raw differential yield ratios $\rho(S_{e,\Sigma,z})$ becomes sizable only as $\rho(S_{e,\Sigma})$, or rather $S_{e,\Sigma}(z,\theta)$ has fallen to ca. 70% to 75% of its maximum level. This feature is easy to understand: The exponential attenuation factor in Eq. (1) may be viewed as a probe for testing the height of $S_e(z,\theta)$ in the vicinity of the surface. If the probe has a narrow width compared to $S_e(z,\theta)$, see Fig. 7(a), the ratio r of the integrals $g(\theta,L)$ will differ only very little from the ratio ρ of the differential distributions $S_e(z,\theta)$. Differences can only be expected as L exceeds the width of $S_e(z,\theta)$. (iv) An open question is whether attenuation is exactly exponential. To examine this issue rigorously, the assumption was made that the probability for an excited electron to travel to the surface is constant in the depth interval $0 \leqslant z \leqslant L_{\mathrm{box}}$, thus strongly enhancing emission from large depths. Applying this rather speculative idea to the calculated data for 10-keV O on Mg, L_{box} was found to be only 70% larger than $L \equiv L_{\mathrm{exp}}$. With this result in mind it was not surprising to find that integral yield ratios $g(\theta,L)$, obtained using a theoretically derived, modified exponential attenuation function [7], differed only marginally from the truly exponential case.

Turning now to projectile-target combinations featuring dominant excitation by recoils, Fig. 10(a) shows the results of an attenuation-length exercise for 40-keV Xe on Al [14]. In this case the calculated (total) yield ratios $r(S_{e,\Sigma,L})$ are seen to be up to 50% higher than the ratios $r(S_{e,p,L})$ for projectile excitation only. Evidently agreement between measured and calculated yield ratios is impossible to achieve if only $S_{e,p}$ is taken into account: The measured electron-yield ratios $r(\gamma)$ strongly exceed $r(S_{e,p,L})$. The additional contribution to ionization by recoils must be included, as argued before [7,13–15]. The data shown here may be considered a particularly convincing proof in favor of this reasoning. One may actually go a step further arguing that, according to the results of Fig. 10(b), the contributions due to projectiles and recoils add equally, with no need to apply different "efficiency factors" to either contribution. This can be read as saying that in both cases excitation is largely isotropic.

The L values derived from the results of Fig. 10(a) range between 0.9 and 1.3 nm. Another example illustrating the importance of recoil ionization is presented in Fig. 10(b). The data for 40-keV Cu-Cu are interesting in that potential emission cannot occur because the ionization potential of Cu is too low. L values: 1.4 ± 0.1 nm for Xe-Cu, 1.9 nm for Cu-Cu.

Comparing the results of Figs. 9 and 10 for $\theta = 60^\circ$ and 70° one will note an interesting difference. Whereas in Fig. 9 the calculated yield ratios $r(S_{e,\Sigma,L})$ pass through a broad maximum, these ratios decrease monotonically and comparatively rapidly in Fig. 10. The latter behavior is quite advantageous for the present study in that it allows L to be determined rather safely at 60° (and at even less oblique incidence). The favorable feature is due to the dominant contribution of recoils. As shown in Fig. 3(b), recoil ionization at normal incidence arrives at its maximum only at some depth, distinctly larger than L. Hence, in the depth region of interest, $S_{e,\Sigma}(z,\theta = 0)$ exhibits a pronounced low at and near the surface which causes the electron yield to be relatively low as well. By contrast, for sufficiently oblique incidence, $S_{e,\Sigma}$ has its maximum right at the surface. These two features combined have the effect of considerably enhancing $r(S_{e,\Sigma})$ and $\rho(S_{e,\Sigma})$ near the surface.

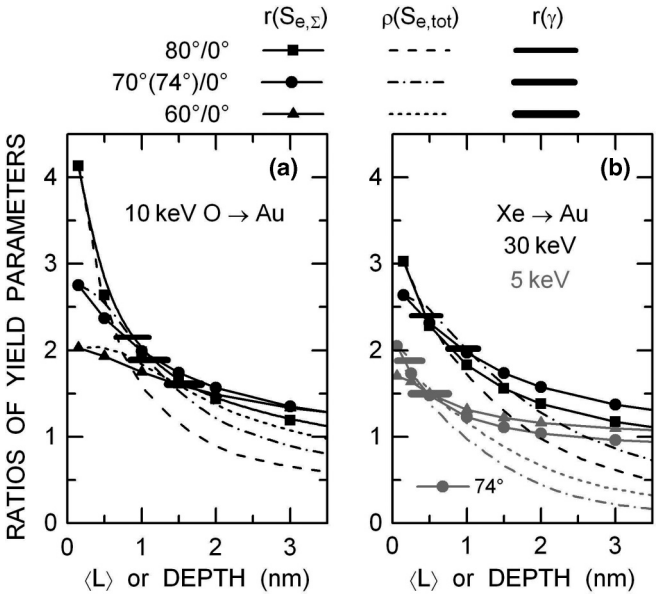

FIG. 12. The same as Fig. 9, but for (a) 10-keV O on Au [13] and (b) 5 and 30-keV Xe on Au. Potential emission considered negligible. Step width in the SRIM calculations 0.12 nm. Note that the total depth covered in the two panels is only 3.5 nm.

The next example addresses cases where electronic excitation extends to large depths, notably at impact angles $\theta \leqslant 70°$. In Fig. 11 yield ratios are compared for He on Cu at two different energies, 20 and 50 keV. The data are interesting because the angular dependence of electron yields was found to be (inversely) over cosine at angles up to 80° [13]. Owing to the large depth of electronic excitation at moderately oblique projectile incidence, L can be determined reasonably safely only at impact angles as large as 80°, $L = 1.4\pm0.3$ nm. The data at less oblique incidence are nevertheless quite useful in that they can serve to test how well the calculated maximum yield ratios agree with measured yield ratios.

Finally, examples of very shallow excitation deserve attention. Results for 10-keV O on Au and 5- and 30-keV Xe on Au are presented in Fig. 12. In these cases the derived (apparent) L values are seen to be often unusually low and to decrease strongly with increasing impact angle. The origin of this effect is not too difficult to identify: For $\theta \geqslant 70°$, the distributions of electronic excitations are located so close to the surface that most of the "action" takes place at distances from the surface less or even much less than L. If the depth of major excitation becomes smaller than L, a sizable fraction of the total depth from which ejected electrons could originate is not utilized. Such data are not suited to determine L. One should also note that, for shallow excitation, even the maximum differential yield ratio can fall below the $1/\cos\theta$ reference level, as already discussed with reference to Fig. 8. In other words, excitation in the depth region $0 \leqslant z \leqslant L$ is so weak that the electron yields are much smaller than they were if excitation would extend to larger depth. This is the origin of the differences in the angular dependence of $\gamma(\theta)$ seen in Fig. 1 for different projectile-target combinations and impact energies.

IV. CONCLUSION

This study has provided evidence that the observed angular dependence of ion-induced kinetic electron emission can be explained assuming that the yields are controlled by the depth distributions of electronic energy deposition and a characteristic depth of emission, referred to as the mean attenuation length L. The very remarkable result of this work is that the calculated energy deposition data allow angular-dependent electron yields from three different sources, covering a wide range of projectile-target combinations and impact energies, to be rationalized in an internally consistent manner. Quantitative agreement between measured and calculated yield ratios was obtained if the mean attenuation length is set to $L = 1.5\pm0.3$ nm. The derived L value in this study falls into the margin that one might expect from recent measurements of the IMFP [11,12] in combination with estimates of the low-energy elastic mean free path [10]. By contrast, attenuation lengths as large as 10–15 nm were recently advocated to explain the very high electron yields measured in studies on internal KEE in metal-insulator-metal sandwich layers [18–20]. With $L = 1.5$ nm and a top layer thickness of typically 15 nm, the internal yields should be unmeasurably small. Alternatively, if L were as large as 10 nm or more in standard (external) KEE studies, the angular dependence of electron yields would be much weaker than observed, with yields even decreasing with increasing impact angle for shallow excitation. At this point it is impossible to bridge the tremendous gap between the cited internal yield studies and results presented here.

[1] W. O. Hofer, *Scanning Microsc.* **4**, 265 (1990).
[2] D. Hasselkamp, in *Particle Induced Electron Emission II* (Springer, New York, 1992).
[3] R. A. Baragiola, Nucl. Instrum. Methods Phys. Res., Sect. B **78**, 223 (1993).
[4] N. Bajales, S. Montoro, E. C. Goldberg, R. A. Baragiola, and J. Ferrón, Surf. Sci. **579**, L97 (2005).
[5] M. Commisso, M. Minniti, A. Sindona, A. Bonanno, A. Oliva, R. A. Baragiola, and P. Riccardi, Phys. Rev. B **72**, 165419 (2005).
[6] S. Tanuma, C. J. Powell, and D. R. Penn, Surf. Interface Anal. **17**, 911 (1991).
[7] S. Tougaard and P. Sigmund, Phys. Rev. B **25**, 4452 (1982).
[8] W. H. Gries and W. Werner, Surf. Interface Anal. **16**, 149 (1990).
[9] A. Jablonski and C. J. Powell, Surf. Sci. Rep. **47**, 33 (2002).
[10] P. J. Cumpson and M. P Seah, Surf. Interface Anal. **25**, 430 (1997).
[11] J.D. Bourke and C.T. Chantler, Phys. Rev. Lett. **104**, 206601 (2010).

[12] R. Zdyb, T.O. Mentes, A. Locatelli, M.A.Niño, and E. Bauer, Phys. Rev. B **87**, 075436 (2013).
[13] J. Ferrón, E. V. Alonso, R. A. Baragiola, and A. Oliva-Florio, Phys. Rev. B **24**, 4412 (1981).
[14] B. Svensson and G. Holmén, J. Appl. Phys. **52**, 6928 (1981).
[15] B. Svensson, G. Holmén, and A. Burén, Phys. Rev. B **24**, 3749 (1981).
[16] K. Wittmaack, Nucl. Instrum. Methods Phys. Res., Sect. B **115**, 288 (1996).
[17] M. A. Karolewski and R. G. Cavell, Surf. Sci. **605**, 1842 (2011).
[18] S. Meyer, C. Heuser, D. Diesing, and A. Wucher, Phys. Rev. B **78**, 035428 (2008).
[19] D. Kovacs, A. Golczewski, G. Kowarik, F. Aumayr, and D. Diesing, Phys. Rev. B **81**, 075411 (2010).
[20] C. Heuser, M. Marpe, D. Diesing, and A. Wucher, Nucl. Instrum. Methods Phys. Res., Sect. B **269**, 1190 (2011).
[21] J. F. Ziegler, M. D. Ziegler, and J. P. Biersack, The Stopping and Range of Ions in Matter, www.srim.org.
[22] K. Wittmaack, J. Appl. Phys. **96**, 2632 (2004).
[23] P. Sigmund, Euro. J. Phys. D **47**, 45 (2008).
[24] Y. Zhang, I.-T. Bae, K. Sun, C. Wang, M. Ishimaru, Z. Zhu, W. Jiang, and W.J. Weber, J. Appl. Phys. **105**, 104901 (2009).
[25] J. Lindhard, M. Scharff, and H. E. Schiøtt, K. Dan. Vidensk. Selsk., Mat. Fys. Medd. **33**, 14 (1963).
[26] K. Wittmaack, Appl. Phys. A **38**, 235 (1985).
[27] L. M. Kishinevsky, Radiat. Eff. Defects Solids **19**, 23 (1973).